

Tailoring microcombs with inverse-designed, meta-dispersion microresonators

Received: 5 October 2022

Accepted: 14 June 2023

Published online: 17 July 2023

 Check for updatesErwan Lucas^{1,2,4}✉, Su-Peng Yu^{1,2}, Travis C. Briles¹, David R. Carlson^{1,3} & Scott B. Papp^{1,2}✉

Nonlinear wave mixing in optical microresonators offers new perspectives to generate compact optical-frequency microcombs, which enable an ever-growing number of applications. Microcombs exhibit a spectral profile that is primarily determined by their microresonator's dispersion. One example is the sech^2 spectrum of dissipative Kerr solitons under anomalous group-velocity dispersion. Here we introduce an inverse-design approach to spectrally shape microcombs, by optimizing an arbitrary meta-dispersion in a resonator. By incorporating the system's governing equation into a genetic algorithm, we are able to efficiently identify a dispersion profile that produces a microcomb closely matching a user-defined target spectrum, such as spectrally flat combs or near-Gaussian pulses. We show a concrete implementation of these intricate optimized dispersion profiles, using selective bidirectional-mode hybridization in photonic-crystal resonators. Moreover, we fabricate and explore several microcomb generators with such flexible 'meta' dispersion control. Their dispersion is not only controlled by the waveguide composing the resonator, but also by a corrugation inside the resonator, which geometrically controls the spectral distribution of the bidirectional coupling in the resonator. This approach provides programmable mode-by-mode frequency splitting and thus greatly increases the design space for controlling the nonlinear dynamics of optical states such as Kerr solitons.

Microcombs—optical-frequency combs generated in driven Kerr resonators¹—are versatile light sources that offer unique properties for applications and integration of frequency-comb systems on a chip. Through experimentation and advances in the fabrication of integrated resonators, microcombs have progressed from a theoretical framework for Kerr-nonlinear optics^{2,3} to the generation of octave-spanning combs for accurate and precise optical metrology⁴. The large mode spacing and spectral width of microcombs have already found applications in parallel coherent communication⁵, distance measurement^{6–8} and phase stabilization⁹ for photonic-integrated frequency synthesis⁴.

Microcomb generation often entails the formation of dissipative Kerr solitons (DKSs)^{10,11}, which exist by balancing losses from nonlinear

gain, anomalous group-velocity dispersion (GVD) and pump-laser detuning, through nonlinear phase shifts. Dominated by second-order dispersion, the resulting DKS pulses feature a squared secant hyperbolic profile in the time and frequency domains (Fig. 1a). Owing to this equilibrium with the Kerr nonlinearity, the dispersion of the resonator—or more generally mode-by-mode frequency mismatch from the resonator's free-spectral range (FSR)—primarily determines the pulse shape and spectrum of nonlinear states it supports.

Tailoring the comb spectral profile is desired in applications such as telecommunications, where high power per mode and spectral flatness improve the performance and efficiency of data links. However, there is currently no direct relationship connecting the desired microcomb spectrum with the required dispersion, material

¹Time and Frequency Division, National Institute of Standards and Technology, Boulder, CO, USA. ²Department of Physics, University of Colorado, Boulder, CO, USA. ³Octave Photonics, Louisville, CO, USA. ⁴Present address: Laboratoire ICB, UMR CNRS 6303, Dijon, France.

✉e-mail: erwan.lucas@polytechnique.org; scott.papp@nist.gov

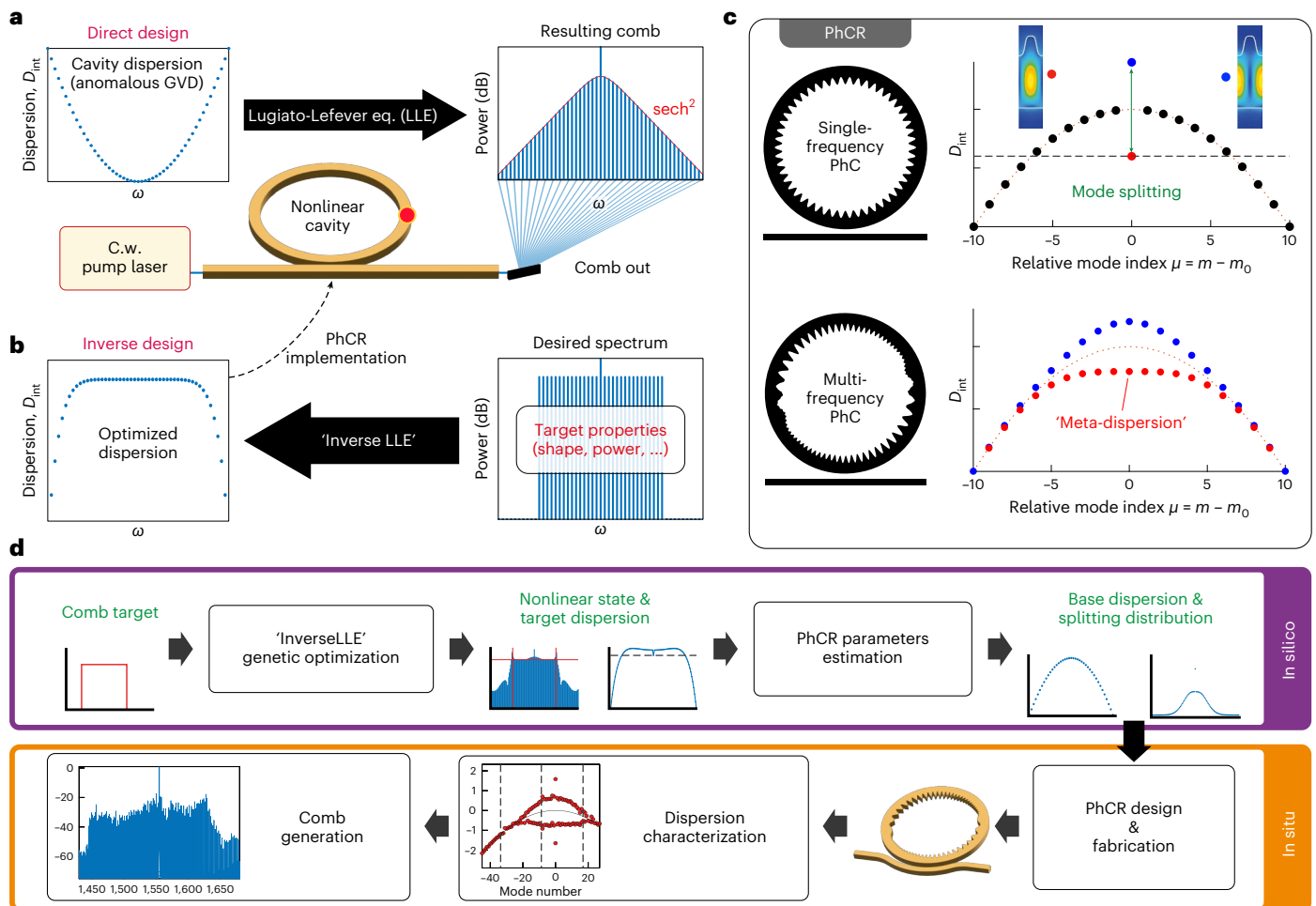


Fig. 1 | Concept of microcomb inverse design via meta-dispersion engineering. **a**, Microcomb generation in an optical microresonator. The resonator dispersion determines the comb spectral envelope, following the Lugiato–Lefever equation (LLE). Applying this nonlinear model, knowing the resonator parameters, can be viewed as direct design. **b**, The concept of inverse design consists of the reverse operation, that is, assignment of a desired comb envelope and determination of the optimal microresonator dispersion for which the resulting comb shape is closest to the target. This ‘inverse LLE’ is accomplished here with a GA. The optimized dispersion profiles are implemented using PhCRs. **c**, A PhCR is a microring resonator where the inner ring waveguide wall is patterned with a subwavelength modulation ($\lambda/2$). This leads to targeted and tunable single mode splitting, with the formation of a red- and blueshifted pair of modes (respectively shifted to lower and higher frequency). The PhCR approach can be generalized to split multiple modes simultaneously by superposing several modulation patterns (bottom panel). The combined effects of waveguide dispersion and mode splitting create a composite dispersion, or meta-dispersion, on the blue- and redshifted branches. **d**, Our procedure for tailoring microcombs consists of several steps. A desired comb shape is first defined. A GA calculates the optimized dispersion profile, which is then converted into meta-dispersion parameters, determining the geometry of the PhCR. The devices are nanofabricated and characterized, before pumping the suitable resonators.

This leads to targeted and tunable single mode splitting, with the formation of a red- and blueshifted pair of modes (respectively shifted to lower and higher frequency). The PhCR approach can be generalized to split multiple modes simultaneously by superposing several modulation patterns (bottom panel). The combined effects of waveguide dispersion and mode splitting create a composite dispersion, or meta-dispersion, on the blue- and redshifted branches. **d**, Our procedure for tailoring microcombs consists of several steps. A desired comb shape is first defined. A GA calculates the optimized dispersion profile, which is then converted into meta-dispersion parameters, determining the geometry of the PhCR. The devices are nanofabricated and characterized, before pumping the suitable resonators.

properties or physical geometry of the resonator. Additionally, achieving precise dispersion control in resonators has historically been a substantial challenge, lacking a demonstrated technique for imparting arbitrary dispersion properties. Nevertheless, recent advances in numerical computation and machine learning have introduced new capabilities and tools for system design and optimization^{12–15}. Integrated photonics, meanwhile, not only offers potential for the miniaturization of large-scale systems, but also allows greater control over guided modes of light, particularly in photonic crystals¹⁶, or topology-optimized elements^{17,18}, which have paved the way to highly customizable inverse-designed microresonators¹⁹.

In this Article we propose and implement an inverse-design process to shape the spectral envelope of microcombs. Our approach numerically optimizes an arbitrary dispersion profile to tailor the associated nonlinear state of the resonator towards a target pulse shape and spectrum. The resulting complex dispersion relation is then implemented indirectly by means of photonic-crystal resonators (PhCRs), where the resonance frequencies can be controlled

via multiple selective mode splitting^{20–22} to create a meta-dispersion (Fig. 1c). We demonstrate a full iteration of the design process and first experimental evidence of microcomb shaping. The design steps followed in our work are summarized in Fig. 1d. First, we numerically solve the governing equation of the resonator and use a genetic algorithm (GA) to iteratively optimize the dispersion and pumping parameters to create a desired microcomb shape. Although a similar GA-based method has been developed concurrently²³, our approach notably introduces an analytical model based on the target comb’s Kerr shift to efficiently generate an initial dispersion. Second, we determine the PhCR topology needed to achieve the optimized dispersion. Finally, we demonstrate realizations of meta-dispersion in PhCR microresonators and initial observations of comb generation in these devices.

Results

Inverse-design dispersion optimization

We first describe our precise formalism and notation. The Lugiato–Lefever equation² (LLE) accurately models the driven nonlinear

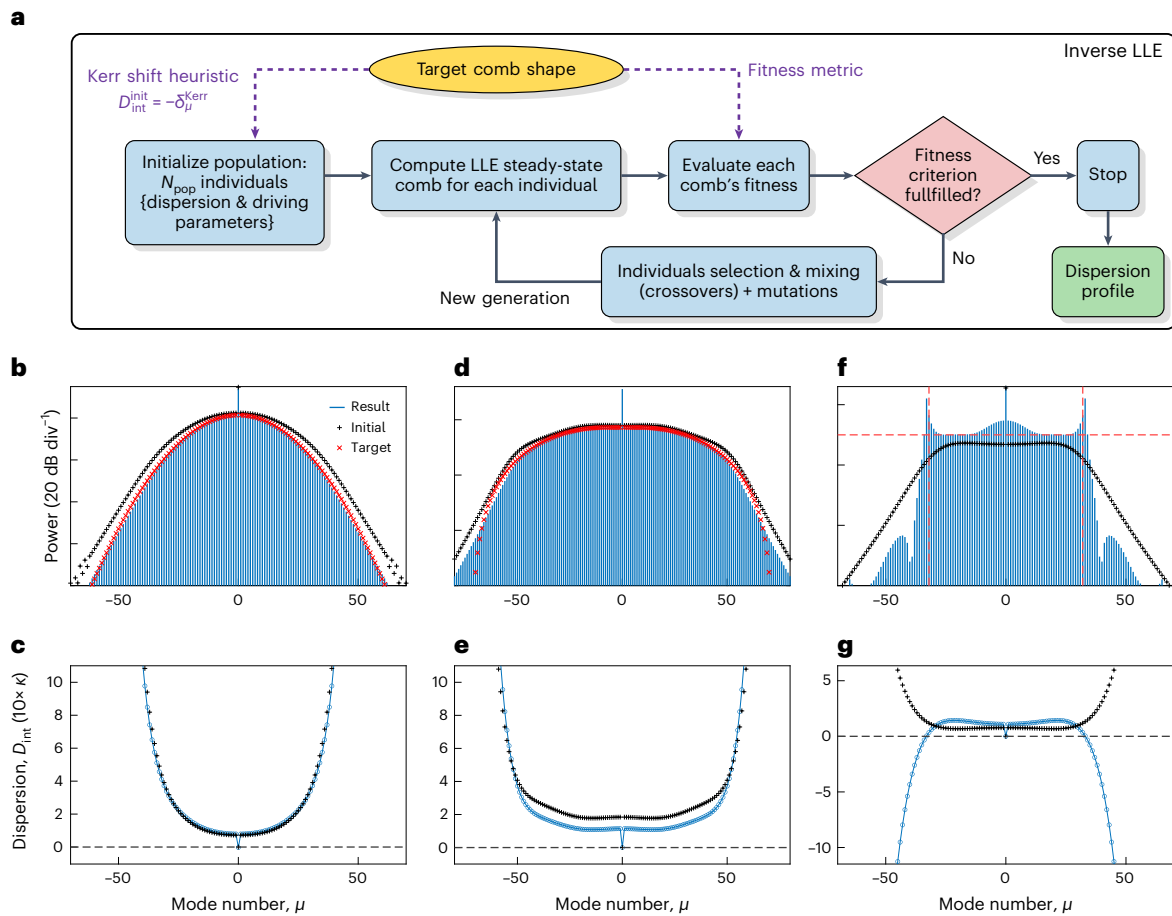


Fig. 2 | Dispersion optimization for comb shaping. **a**, Flowchart of the evolutionary algorithm used to optimize the dispersion and driving parameters to match a given comb spectral profile. **b**, Comb spectra of a targeted Gaussian comb envelope (red), the initial comb profile computed from the Kerr shift initialization (black) and the evolutionary algorithm result (blue). The driving parameters $\{2\delta\omega/\kappa, P_{in}/P_{th}\}$ are initially $\{4.4, 13\}$ and $\{5, 8.6\}$ after optimization. **c**, Computed Kerr-shift-based initialization (black crosses) and the integrated dispersion profile after evolutionary optimization (blue). **d**, Set of comb spectra

for a targeted raised-cosine shape ($\beta = 0.8$; Methods): initial driving $\{4.4, 13\}$ and optimized set $\{6.5, 11.7\}$ (key as in **b**). **e**, Corresponding dispersion for the spectra shown in **d** (colours as in **c**). **f**, Optimization with the objective of reaching a minimum power-per-line requirement over a given bandwidth: initial driving $\{3.5, 7\}$ and optimized set $\{1.2, 7\}$ (key as in **b**). **g**, Corresponding dispersion for the spectra shown in **f** (colours as in **c**). Although the initial dispersion is in the anomalous regime, the optimized dispersion is mainly normal.

resonator and can be written as a set of coupled mode equations in the spectral domain:

$$\frac{\partial \bar{A}_{\mu}}{\partial t} = -\left[\frac{\kappa}{2} + i(\delta\omega - D_{int}(\mu))\right] \bar{A}_{\mu} + i g_0 \mathcal{F}[|A|^2 A]_{\mu} + \sqrt{\kappa_{ex} \frac{P_{in}}{\hbar\omega_0}} \delta_{\mu=0} \quad (1)$$

where μ is the azimuthal mode number relative to the pumped mode, $|\bar{A}_{\mu}(t)|^2$ is the number of photons in mode μ as a function of the ‘slow’ time t , P_{in} and $\delta\omega = \omega_0 - \omega_{pump}$ are respectively the pump power and detuning terms¹¹ (the detuning is positive if the laser frequency is lower than the resonance frequency), κ is the resonator full-width at half-maximum (FWHM) linewidth, and κ_{ex} is the coupling rate. $\mathcal{F}[\cdot]_{\mu}$ represents the Fourier series operator and g_0 the per-photon Kerr shift of the resonator modes. $P_{th} = \hbar\omega_0\kappa^3/8g_0\kappa_{ex}$ is the threshold pump power for initial four-wave mixing in resonators and is useful to rescale the power quantities. The operator $D_{int}(\mu) = (\omega_{\mu} - \omega_0) - D_{\mu}$ represents the resonator dispersion²⁴ and measures the deviation of the resonance frequencies from an equidistant FSR, D_1 .

Optimization problem. The dispersion plays a key role in determining the temporal and spectral shape of localized structures emerging from

nonlinear effects in a resonator. One problem of interest is to find the dispersion D_{int} of the resonator that yields a comb with desired properties, and is a steady-state solution of the LLE (Fig. 1b).

To simplify the problem, we describe the dispersion using a set of polynomial coefficients D_k such that $D_{int}(\mu) = \sum_{k=2}^8 \frac{D_k}{k!} \mu^k + \frac{\gamma_0}{2} \delta_{\mu=0}$. The extra degree of freedom, γ_0 , corresponds to a discrete shift in the frequency of the pump mode, which is known to favour the formation of pulses, notably in the normal-dispersion regime^{20,25,26}. An additional constraint limits the pump power within a specified budget of P_{max} . Our objective is to determine the values of D_k , γ_0 , $\delta\omega$ and P_{in} that result in a stationary comb profile that best satisfies our objective, as quantified by the error function $\mathcal{E}(\bar{A}_{\mu})$ (see Methods for details). To solve this optimization problem, we use a genetic evolutionary algorithm^{23,27,28}.

Initialization. It is useful to leverage prior knowledge to initialize the problem as closely as possible to a potential solution. An initial dispersion profile is first derived based on a simple heuristic, inspired by the essential principle of the soliton balance of dispersion by the Kerr shift. Thus, in the frequency domain, the dispersion $D_{int}^{initial}(\mu)$ is initialized as the opposite of the Kerr spectral shift δ_{μ}^{Kerr} of the target comb state \bar{A}_{μ}^{target} , according to²⁰

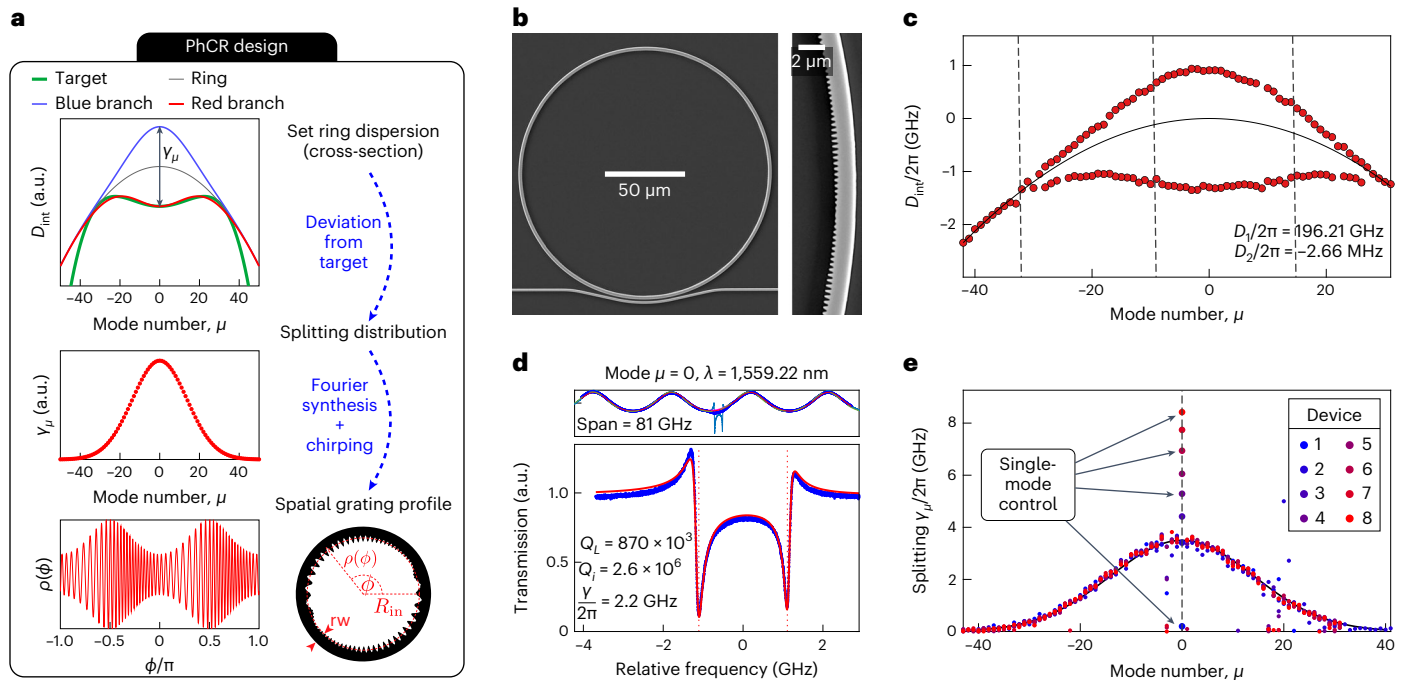


Fig. 3 | Meta-dispersion in PhCRs. **a**, Design principle of the meta-dispersion PhCRs. First, the resonator dispersion is chosen to match the dominant sign of the targeted dispersion returned by the GA, which sets the waveguide cross-section. The spectral distribution of mode splitting is then set equal to twice the deviation between the target dispersion and that of the waveguide near the central modes. Finally, the required grating profile is generated by Fourier synthesis. The various components of the grating are superposed with a chirp to distribute the grating modulation more evenly along the ring. **b**, SEM image of a meta-dispersion PhCR. The inset on the right highlights a section of the chirped corrugation. **c**, Measured integrated dispersion of a PhCR ($r_w = 2.3 \mu\text{m}$,

$t_h = 570 \text{ nm}$). The designed splitting profile follows a Gaussian curve. **d**, Fitting of the split resonance of mode $\mu = 0$. The asymmetric lineshape⁴¹ originates from interference with the chip Fabry–Pérot (facets reflections) fitted on the top panel. A mode-splitting model⁴² is then fitted to the PhCR resonance to extract the loaded and intrinsic quality factors (Q_L , Q_i) and splitting parameters (lower panel). **e**, Distribution of mode splitting retrieved from fitting the resonances of several PhCR devices. The splitting distributions are designed with the same Gaussian profile, where only the splitting of the zeroth mode is varied from device to device. Single-mode control of the splitting is maintained.

$$D_{\text{int}}^{\text{init}}(\mu) = -\delta_{\mu}^{\text{Kerr}} = -\Re \left(\frac{\mathcal{F} \left[|A^{\text{target}}|^2 A^{\text{target}} \right]_{\mu}}{\bar{A}_{\mu}^{\text{target}}} \right) \quad (2)$$

This relation is hence fitted with a polynomial to obtain the initial dispersion coefficients. The pump-laser parameters (P_{in} , $\delta\omega$) are also initialized, below P_{max} for the former and based on the maximum single-mode Kerr shift for the latter²⁹. A population of dispersion candidates, with a typical size of $N_{\text{pop}} = 208$, is then generated from random variations around these initial parameters.

Evolution step. The GA loop for finding the optimal parameters consists of two steps, as presented in Fig. 2a. First, the steady-state intra-resonator field is computed for each member of the population by integrating the LLE equation via split-step Fourier transform. Next, the steady-state comb solutions are ranked based on an error function $\mathcal{E}(\bar{A}_{\mu})$ that measures their fitness for the optimization goal. This metric can be the mean square error to a target comb shape or a binary criterion that checks whether a given power target is reached for certain lines. To ensure stable and low-noise combs, highly fluctuating states are penalized. If a solution meets a fitness threshold or a maximum generation number is reached, the algorithm stops. Otherwise, a new population is created by combining two parents’ dispersion coefficients (crossover) and adding a random variation (mutation) to generate each new candidate, before the loop continues. The GA is further detailed in the Methods.

Optimization results. First, we show how the dispersion can be optimized to obtain a comb with nearly Gaussian spectral profile in the resonator. Figure 2b shows the target comb, the initial comb and the result after optimization. The initial dispersion profile, shown in Fig. 2c, is calculated from the target comb Kerr shift using equation (6). The optimized dispersion appears almost identical to this initial profile. The GA mainly modified the pumping conditions to fit the spectral width to the target.

For applications, such as telecommunications, a flat microcomb with high conversion efficiency and maximum power per line is typically required. Using a rectangular comb target is problematic as the function is discontinuous. A raised-cosine shape makes a more realistic target for optimization as it has a smoother decay outside the bandwidth of interest, as shown in Fig. 2d. Moreover, the regularity of the function makes it possible to compute the Kerr shift, which again provides an excellent starting point (Fig. 2e). The GA mainly modifies the pump mode shift γ_0 and the driving parameters. These examples demonstrate that our method can perform a ‘fitting’ of a specific comb target by changing the parameters of the LLE. Our initialization technique also proves to be very effective in coarsely matching a desired comb shape, which can speed up the convergence of the GA, especially if it preferentially adjusts the pumping parameters. An exhaustive search could even be conducted.

An alternative approach to obtain efficient flat comb generation is to modify the fitness metric to enforce a comb line power of at least P_{min} over a given bandwidth (Methods). We initialize the dispersion from the Kerr shift of a flat-top comb model (Methods), which does not satisfy the power criterion, although we sought to obtain the highest

possible power. After optimization, the power criterion is met by the resulting comb, as shown in Fig. 2f. Interestingly, the associated dispersion profile, shown in Fig. 2g, is dominantly normal for higher relative mode number, and turns locally anomalous near the pump mode. The general comb shape resembles the typical ‘platonic’ spectrum obtained in normal dispersion^{25,26,30}, that is, a strong central lobe surrounded by two pronounced wings, which is known to have high conversion efficiency³¹. However, the centre lobe here has a flattened sech-like profile¹¹. In this optimization problem, where the target comb is not provided, the GA plays a prominent role, because it extensively explores the parameter space and converges to a radically different solution from the initialization. Overall, the heuristic approach and the GA are complementary tools in the inverse-design process. The former can be used to quickly obtain a rough estimate of the optimal parameters in specific problems, whereas the latter can refine the parameters and explore a broader range of solutions. Finally, it should be noted that the algorithm does not guarantee to find a global optimum to the problem. However, we tested the convergence robustness by repeating this optimization problem three times, and obtained similar dispersion profiles for all iterations.

An additional scenario, targeting enhanced dispersive-wave emission, is discussed in the first section of the Supplementary Information. Before finalizing the meta-dispersion design, bidirectional LLE simulations³² are performed, with sweeps of $\delta\omega$, P_{in} and γ_0 to ensure that the desired nonlinear state can be achieved in the resonator, under realistic driving conditions (Supplementary Section 3 provides details).

Meta-dispersion

The complex dispersion obtained with the GA is realized by means of engineered mode splittings in a PhCR (Fig. 1c). A distributed corrugated grating is fabricated on the inner wall of a ring resonator, introducing a clockwise–anticlockwise coupling and hence a mode hybridization. The corrugation’s period and amplitude respectively control the impacted longitudinal mode and the splitting amplitude. By appropriately superposing multiple corrugations, we generalize this concept to simultaneously control multiple dozens of modes, while faithfully retaining a designed spectral distribution of mode splitting, γ_μ . The combined ring waveguide dispersion and mode-splitting distribution define an effective synthetic dispersion, or meta-dispersion, on the blue- and redshifted branches, corresponding to the up- and down-frequency-shifted split modes.

PhCR design. Figure 3a shows the implementation of the optimization result using meta-dispersion. The dispersion is decomposed into two components. First, the ring’s dispersion is chosen to match the general sign of the optimized dispersion at high mode numbers, which allows us to set the waveguide’s cross-section. The mode-splitting spectral distribution γ_μ near the central modes is then taken as twice the difference between the target dispersion and that of the waveguide, so that one of the shifted branches coincides with the target dispersion. Finally, the corrugation’s azimuthal profile $\rho(\phi)$ is calculated by use of Fourier synthesis of this distribution:

$$\rho(\phi) = \sum_{\mu \in \mathbb{Z}} \frac{\tilde{\rho}_\mu}{2} \cos(2(m_0 + \mu)\phi + \xi\mu^2) \quad (3)$$

where the modulation amplitude $\tilde{\rho}_\mu$ is determined based on an experimental calibration of the frequency splitting versus PhC amplitude relation $\gamma(\rho)$ (Methods). m_0 is the ‘carrier’ modulation that sets the azimuthal mode index of the central mode, $\mu = 0$.

Importantly, the various frequency components of the grating are superposed with a phase offset (chirp ξ) to distribute the corrugation’s amplitude evenly across the ring perimeter. This minimizes the corrugation peak amplitude and preserves the shape of the desired splitting distribution. Indeed, because we use the fundamental transverse

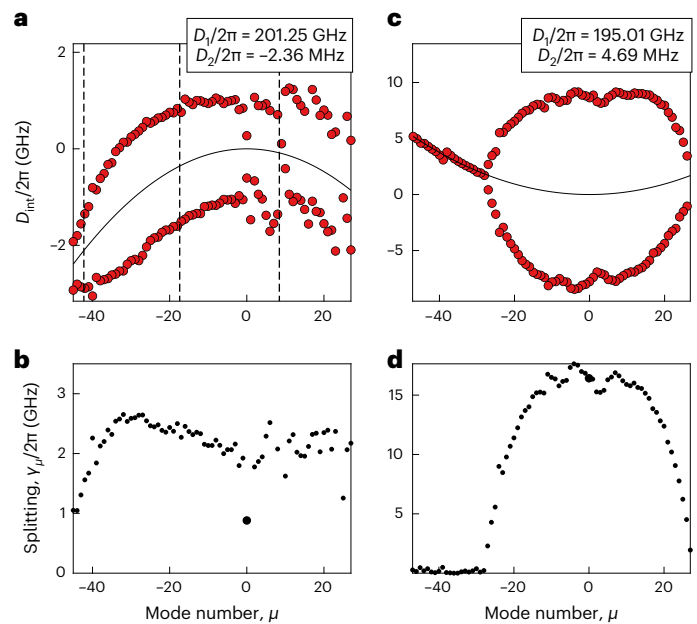


Fig. 4 | Examples of meta-dispersion in PhCR. **a**, Normal dispersion ring with flattening of the blueshifted (upper) branch. The impact of the avoided mode crossings with higher-order mode families is causing the disruptions near $\mu = 10$. **b**, Corresponding mode-splitting distribution. **c**, Anomalous dispersion ring ($rw = 1.3 \mu\text{m}$) and engineering of the redshifted branch to replicate the profile in Fig. 2c. **d**, Corresponding mode-splitting distribution.

electric mode of the waveguide, which has the highest quality (Q) factor, the relationship $\gamma(\rho)$ is non-monotonic. A similar dispersion control approach was developed concurrently in ref. 22, using the transverse magnetic mode, for which $\gamma(\rho)$ is monotonic.

Characterization. We fabricated the designed devices in a 570-nm-thick Ta_2O_5 (tantala) layer on thermal silicon oxide, without top cladding (see ref. 33 for the fabrication details). The ring resonator baseline dispersion was controlled by changing the width of the waveguide (rw). The resonator FSRs were selected as 200 or 400 GHz. Figure 3b presents a scanning electron microscopy (SEM) image of a completed PhCR, revealing the corrugation pattern.

The dispersion and quality factors were characterized by use of a scanning laser spectroscopy method³⁴, and the resonances frequencies were detected and the integrated dispersion D_{int} retrieved. We first performed a meta-dispersion demonstration with a Gaussian splitting profile in a normal-dispersion ring, shown in Fig. 3c. The integrated dispersion D_{int} illustrates the deviation of each frequency-splitting branch from the continuous resonator dispersion. The resonance pair for each longitudinal split mode was fit with a model to recover the characteristics of the resonances. Thus, we found that adding the corrugation does not degrade the Q factor for modulation depths under 10% of the ring width. The splitting spectral profile γ_μ was also retrieved and shows a Gaussian shape, in excellent agreement with the design.

This characterization was repeated for several resonators, in which only the zeroth mode splitting was changed. Their respective splitting distributions are reported in Fig. 3e, which shows first the excellent reproduction of the global Gaussian profile across the devices. Second, we observed that single mode splitting control is accurately retained, in spite of splitting multiple tens of adjacent modes.

Figure 4 shows further examples of meta-dispersion demonstrations, with various configurations of base ring dispersion (normal and anomalous) and to tailor the dispersion of the red- or blueshifted

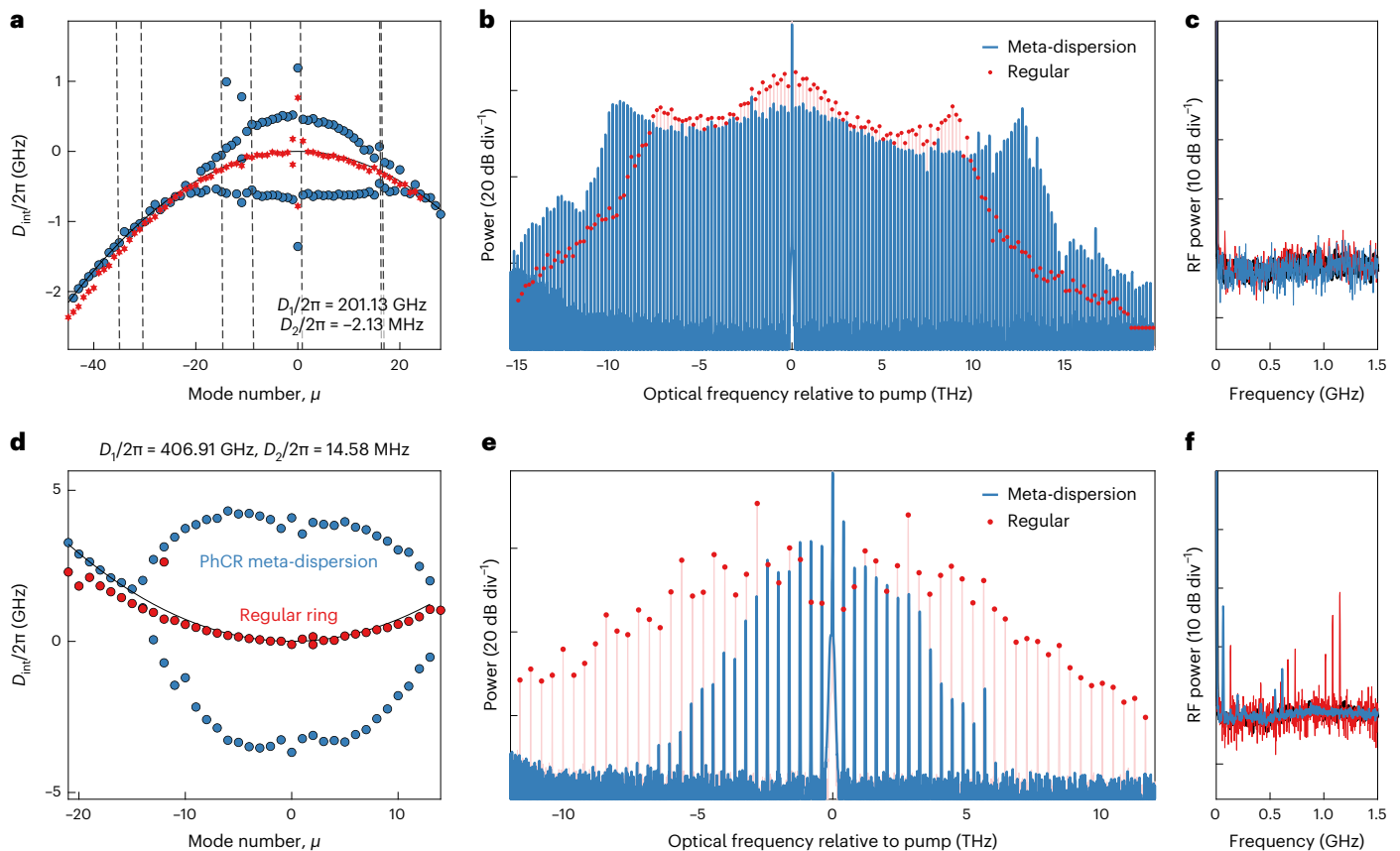


Fig. 5 | Comb generation in meta-dispersion PhCRs. **a**, Measured integrated dispersion. The meta-dispersion resonator (in blue) features a flattened and slightly anomalous dispersion near the centre modes (on the down-shifted branch), in an overall normal-dispersion ring. A normal-dispersion ring with a single mode splitting at $\mu = 0$ that allows comb generation is shown in red. **b**, Optical-frequency comb measured on an optical spectrum analyser, obtained in the meta-dispersion resonator (blue) and regular PhCR (red). The on-chip pump power is 55 mW and 56 mW, respectively. **c**, The intensity noise of the

combs shown in **b** (blue, red) coincides with the electrical spectrum analyser's noise floor (black), confirming a coherent mode-locked state. **d**, Integrated dispersion of a PhCR microresonator for Gaussian-shaped comb generation (blue), compared with a regular ring with anomalous GVD (red). **e**, Comb states generated in each ring (PhCR in blue, regular in red), in the noisy modulation instability regime. The pump powers are 91 mW and 89 mW, respectively. **f**, Intensity noise of the combs shown in **e**. The peaks indicate MI instabilities.

branch. The principle works remarkably well in all cases, such as flattening the blueshifted branch or carving a localized stronger dispersion. Deviations from the measured profiles are nevertheless observed, caused by avoided mode crossing. These are due to the presence of higher-order modes in the resonator and can be problematic for the formation of DKSs³⁵.

Comb generation

We conducted comb generation experiments in PhCR structures with meta-dispersion profiles for two configurations of target comb spectra. To initiate comb generation, the laser power was increased, and its frequency was swept through the redshifted resonance of the split mode $\mu = 0$, starting from the centre of the split and increasing the laser wavelength.

The first configuration targeted a comb with a minimum comb line power. The measured dispersion, shown in Fig. 5a, corresponds to that of a normal-dispersion ring resonator ($rw = 2.3 \mu\text{m}$, radius $109 \mu\text{m}$) with a slight anomalous meta-dispersion near the pump, to reproduce the optimized design shown in Fig. 2g. The device was pumped with 55 mW on-chip. The detuning was first increased to trigger the formation of an initial comb state and then reduced (backward tuning) to induce switching into the state shown in Fig. 5b. The spectrum is analogous to a platicon comb²⁵, but with a flattened centre lobe compared to a single PhC device (shown in red in Fig. 5b), and a wider bandwidth for the same

pump power and base ring dispersion. The number of consecutive teeth within the 5-dB bandwidth is increased from -20 to -50 . Notably, the power per line in the central lobe is lower than in the wings, as featured in the predicted inverse-design comb in Fig. 2f. We confirmed that this comb is a low-noise state by recording its intensity noise, which coincides with the instrument's noise floor (Fig. 5c). Several comb state transitions and breathing stages were observed by changing the power and detuning (Supplementary Fig. 3), revealing complex dynamics.

The second configuration aims at generating Gaussian-shaped combs. The ring features anomalous base dispersion ($rw = 1.55 \mu\text{m}$, radius $53 \mu\text{m}$), and the meta-dispersion is chosen to replicate the computed optimized dispersion in Fig. 2c over a limited range of the redshifted branch, as shown in Fig. 5d. This meta-dispersion PhCR device is compared to a regular ring resonator with the same geometry to provide a baseline for comparison. Figure 5e shows the combs produced in each resonator in the unstable modulation instability (MI) regime, when pumping with ~ 90 mW on-chip. We also ensured that the comb states have comparable intensity noise properties and are in the same stage of MI (subcomb merging³⁶). The regular ring produces a typical MI comb, with powerful comb lines surrounding the pump (corresponding to primary lines) and a dip in comb-line power near the pump. The meta-dispersion resonator exhibits a markedly different comb envelope, with a smoother decrease in power from pump to wings. The MI comb bandwidth is also largely reduced, highlighting the impact of the

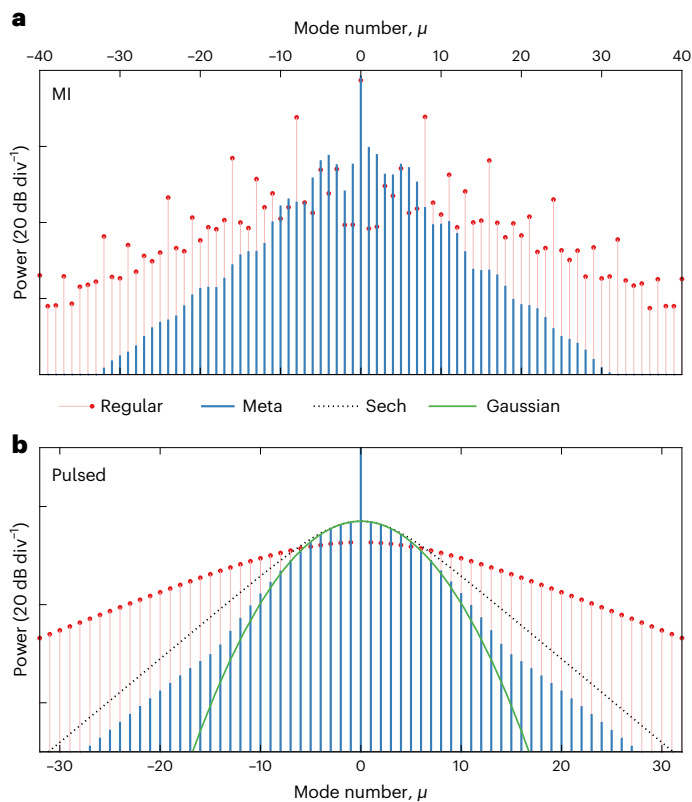


Fig. 6 | Numerical simulation of comb states. **a**, Simulated microcombs in the noisy MI regime, for the PhCR (blue) and regular anomalous GVD ring (red) presented in Fig. 5d. The spectra were averaged over $\sim 130,000$ roundtrips. **b**, Simulation of microcombs in the low-noise pulsed (soliton) regime, for the PhCR (blue) and regular anomalous GVD ring (red). Over the meta-dispersion bandwidth, the PhCR comb features a Gaussian shape (green), as designed.

PhCR in shaping the microcomb. Unfortunately, stable mode-locked soliton states³⁶ could not be obtained in this meta-dispersion device, nor in the regular ring, probably due to the photothermal effect in the cavity^{37,38}, which is particularly strong in Ta₂O₅. The presence of an avoided mode crossing near the pumped mode can also hinder soliton formation³⁵. Therefore, the PhCR comb envelope does not match the expected Gaussian shape, which is obtained in the soliton state, as shown in the following. Nevertheless, we believe that these limitations are not fundamental, but are of technical nature, and that the desired states can be achieved on a more mature technology platform.

Comb simulation. We compared these experimental observations with bidirectional LLE simulations³², as detailed in the Supplementary Section 2. First, we set out to reproduce the comb states in noisy MI to validate our model. The parameters used were taken from the experimental measurements of the resonators shown in Fig. 5d. The detuning was the only adjusted parameter, to recover the unstable MI regime in each resonator. The averaged spectra shown in Fig. 6a are in good agreement with our experimental observations.

Second, because numerical simulations are not subject to thermal effects, they allow us to extrapolate the shape of the stationary ‘mode-locked’ pulsed states in each resonator, which are reached at higher detuning (Supplementary Section 3). The corresponding comb spectra are overlaid in Fig. 6b. The PhCR comb clearly deviates from the usual DKS sech² profile formed in the standard resonator, and follows a Gaussian shape within the meta-dispersion bandwidth. These projections further show that the nonlinear cavity field state is governed by the meta-dispersion.

The results presented here show only the combs co-propagating with the pump. Because the combs are supported by hybrid modes, whose splitting amplitude is substantially larger than the Kerr shift^{20,26}, they are typically generated with near equal power in the clockwise and counterclockwise directions. However, transitions to a dominant direction have been observed, especially when the dispersion is predominantly normal.

Discussion

In summary, we have demonstrated the spectral shaping of microcombs by inverse design, using an optimization layer on the LLE, and we have demonstrated the scalable use of PhCRs for effective meta-dispersion engineering. This flexible approach enables mode-by-mode selectivity and control of nonlinear frequency shifts that are critical in Kerr microcombs. We also showed that meta-dispersion can be used in the nonlinear regime to perform spectral shaping of microcombs.

Further fundamental studies are still needed to fully understand the nonlinear dynamics in hybrid modes, to help control comb formation in these new devices, and to refine our inverse design approach. Moreover, we are considering several ways to enhance our method. The optimization algorithm could occur directly on the meta-dispersion parameters, using the bidirectional LLE within the evolution loop. This nonetheless requires a robust method of seeding the cavity field in both directions. In this respect, machine learning could contribute to speed up the computation, and robustly find the soliton or related nonlinear eigenstates. Other implementations of the optimized dispersion can be conceived, based on coupled resonator chains^{31,39}, through engineered avoided mode crossing with higher-order modes⁴⁰, or by using discrete inverse-designed reflectors¹⁹.

We believe that our comb customization procedure is promising to fully unlock the application potential of microcombs, first in optical telecommunications, where it can maximize the conversion efficiency and the power per line in the bandwidth of interest. In spectroscopy, our concept can help open access to new wavelength ranges, or shape combs that target specific chemical species. Additionally, one could try to optimize the control of the comb parameters (repetition frequency and offset) to improve its intrinsic stability. Finally, the presented method offers new avenues for nonlinear physics, making previously unrealistic dispersion profiles accessible, while contra-propagative coupling promises to produce a myriad of complex dynamics that remain to be explored.

Online content

Any methods, additional references, Nature Portfolio reporting summaries, source data, extended data, supplementary information, acknowledgements, peer review information; details of author contributions and competing interests; and statements of data and code availability are available at <https://doi.org/10.1038/s41566-023-01252-7>.

References

1. Kippenberg, T. J., Gaeta, A. L., Lipson, M. & Gorodetsky, M. L. Dissipative Kerr solitons in optical microresonators. *Science* **361**, eaan8083 (2018).
2. Lugiato, L. A. & Lefever, R. Spatial dissipative structures in passive optical systems. *Phys. Rev. Lett.* **58**, 2209–2211 (1987).
3. Coen, S., Randle, H. G., Sylvestre, T. & Erkintalo, M. Modeling of octave-spanning Kerr frequency combs using a generalized mean-field Lugiato-Lefever model. *Opt. Lett.* **38**, 37–39 (2013).
4. Spencer, D. T. et al. An optical-frequency synthesizer using integrated photonics. *Nature* **557**, 81–85 (2018).
5. Marin-Palomo, P. et al. Microresonator-based solitons for massively parallel coherent optical communications. *Nature* **546**, 274–279 (2017).
6. Trocha, P. et al. Ultrafast optical ranging using microresonator soliton frequency combs. *Science* **359**, 887–891 (2018).

7. Suh, M.-G. & Vahala, K. J. Soliton microcomb range measurement. *Science* **359**, 884–887 (2018).
8. Riemensberger, J. et al. Massively parallel coherent laser ranging using a soliton microcomb. *Nature* **581**, 164–170 (2020).
9. Drake, T. E. et al. Terahertz-rate Kerr-microresonator optical clockwork. *Phys. Rev. X* **9**, 031023 (2019).
10. Leo, F. et al. Temporal cavity solitons in one-dimensional Kerr media as bits in an all-optical buffer. *Nat. Photon.* **4**, 471–476 (2010).
11. Herr, T. et al. Temporal solitons in optical microresonators. *Nat. Photon.* **8**, 145–152 (2013).
12. Lorenc, D., Velic, D., Markevitch, A. & Levis, R. Adaptive femtosecond pulse shaping to control supercontinuum generation in a microstructure fiber. *Opt. Commun.* **276**, 288–292 (2007).
13. Sigmund, O. On the usefulness of non-gradient approaches in topology optimization. *Struct. Multidiscipl. Optim.* **43**, 589–596 (2011).
14. Jensen, J. & Sigmund, O. Topology optimization for nano-photonics. *Laser Photon. Rev.* **5**, 308–321 (2011).
15. Genty, G. et al. Machine learning and applications in ultrafast photonics. *Nat. Photon.* **15**, 91–101 (2021).
16. Joannopoulos, J. D., Villeneuve, P. R. & Fan, S. Photonic crystals: putting a new twist on light. *Nature* **386**, 143–149 (1997).
17. Molesky, S. et al. Inverse design in nanophotonics. *Nat. Photon.* **12**, 659–670 (2018).
18. Yu, Z., Cui, H. & Sun, X. Genetically optimized on-chip wideband ultracompact reflectors and Fabry-Perot cavities. *Photon. Res.* **5**, B15–B19 (2017).
19. Ahn, G. H. et al. Photonic inverse design of on-chip microresonators. *ACS Photonics* **9**, 1875–1881 (2022).
20. Yu, S.-P. et al. Spontaneous pulse formation in edgeless photonic crystal resonators. *Nat. Photon.* **15**, 461–467 (2021).
21. Lu, X., Rao, A., Moille, G., Westly, D. A. & Srinivasan, K. Universal frequency engineering tool for microcavity nonlinear optics: multiple selective mode splitting of whispering-gallery resonances. *Photon. Res.* **8**, 1676 (2020).
22. Moille, G., Lu, X., Stone, J., Westly, D. & Srinivasan, K. Fourier synthesis dispersion engineering of photonic crystal microrings for broadband frequency combs. *Commun. Phys.* **6**, 1–11 (2023).
23. Zhang, C., Kang, G., Wang, J., Pan, Y. & Qu, J. Inverse design of soliton microcomb based on genetic algorithm and deep learning. *Opt. Express* **30**, 44395–44407 (2022).
24. Brasch, V. et al. Photonic chip-based optical frequency comb using soliton Cherenkov radiation. *Science* **351**, 357–360 (2016).
25. Lobanov, V. E., Lihachev, G., Kippenberg, T. J. & Gorodetsky, M. Frequency combs and platicons in optical microresonators with normal GVD. *Opt. Express* **23**, 7713–7721 (2015).
26. Yu, S.-P., Lucas, E., Zang, J. & Papp, S. B. A continuum of bright and dark-pulse states in a photonic-crystal resonator. *Nat. Commun.* **13**, 3134 (2022).
27. Holland, J. H. *Adaptation in Natural and Artificial Systems: An Introductory Analysis with Applications to Biology, Control and Artificial Intelligence* (MIT Press, 1992).
28. Kumar, M., Husain, M., Upreti, N. & Gupta, D. Genetic algorithm: review and application. *SSRN Electron. J.* <https://ssrn.com/abstract=3529843> (2010).
29. Coen, S. & Erkintalo, M. Universal scaling laws of Kerr frequency combs. *Opt. Lett.* **38**, 1790–1792 (2013).
30. Godey, C., Balakireva, I. V., Coillet, A. & Chembo, Y. K. Stability analysis of the spatiotemporal Lugiato-Lefever model for Kerr optical frequency combs in the anomalous and normal dispersion regimes. *Phys. Rev. A* **89**, 063814 (2014).
31. Helgason, Ó. B. et al. Dissipative solitons in photonic molecules. *Nat. Photon.* **15**, 305–310 (2021).
32. Skryabin, D. V. Hierarchy of coupled mode and envelope models for bi-directional microresonators with Kerr nonlinearity. *OSA Continuum* **3**, 1364–1375 (2020).
33. Jung, H. et al. Tantalum Kerr nonlinear integrated photonics. *Optica* **8**, 811–817 (2021).
34. Li, J., Lee, H., Yang, K. Y. & Vahala, K. J. Sideband spectroscopy and dispersion measurement in microcavities. *Opt. Express* **20**, 26337 (2012).
35. Herr, T. et al. Mode spectrum and temporal soliton formation in optical microresonators. *Phys. Rev. Lett.* **113**, 123901 (2014).
36. Herr, T. et al. Universal formation dynamics and noise of Kerr-frequency combs in microresonators. *Nat. Photon.* **6**, 480–487 (2012).
37. Li, Q. et al. Stably accessing octave-spanning microresonator frequency combs in the soliton regime. *Optica* **4**, 193–203 (2017).
38. Gao, M. et al. Probing material absorption and optical nonlinearity of integrated photonic materials. *Nat. Commun.* **13**, 3323 (2022).
39. Ji, Q.-X. et al. Engineered zero-dispersion microcombs using CMOS-ready photonics. *Optica* **10**, 279–285 (2023).
40. Wang, H. et al. Dirac solitons in optical microresonators. *Light Sci. Appl.* **9**, 205 (2020).
41. Fan, S. Sharp asymmetric line shapes in side-coupled waveguide-cavity systems. *Appl. Phys. Lett.* **80**, 908–910 (2002).
42. Gorodetsky, M. L., Pryamikov, A. D. & Ilchenko, V. S. Rayleigh scattering in high-Q microspheres. *J. Opt. Soc. Am. B* **17**, 1051–1057 (2000).

Publisher's note Springer Nature remains neutral with regard to jurisdictional claims in published maps and institutional affiliations.

Springer Nature or its licensor (e.g. a society or other partner) holds exclusive rights to this article under a publishing agreement with the author(s) or other rightsholder(s); author self-archiving of the accepted manuscript version of this article is solely governed by the terms of such publishing agreement and applicable law.

© The Author(s), under exclusive licence to Springer Nature Limited 2023

Methods

Genetic algorithm

Our goal is to find the parameters D_k , γ_0 , $\delta\omega$ and P_{in} that yield a stationary comb profile (for the LLE) \tilde{A}_μ that minimizes an error function $\mathcal{E}(\tilde{A}_\mu)$, which quantifies our objective. The optimization problem can be formalized as follows:

$$\begin{cases} \text{minimize}_{D_k, \gamma_0, \delta\omega, P_{\text{in}}} \mathcal{E}(\tilde{A}_\mu) \\ \text{subject to} \begin{cases} \text{eq. (1)} = 0 \\ P_{\text{in}} \leq P_{\text{max}} \end{cases} \end{cases} \quad (4)$$

The latter term constrains the pump power within a limited power budget. Based on the available power and our resonator's properties, we set $P_{\text{max}} = 13P_{\text{th}}$.

The LLE steady-state field for each member of the population is estimated using split-step Fourier-transform integration⁴³ of equation (1). An initial pulse consisting of an approximate soliton profile³ is seeded in the simulation, and its evolution through the LLE is computed for 100 photon lifetimes. The pump power and detuning are kept constant. Although the stationary state of the LLE can be found using a Newton–Raphson method³, we found that its convergence was slower and less systematic than the split-step approach, especially in complex dispersion profiles.

The steady-state solution of each member of the population is then ranked according to a metric $\mathcal{E}(\tilde{A}, D_k)$, which measures each comb's 'fitness' with respect to the optimization goal. The smaller the error, the more fit the candidate. This metric can be the squared Euclidean distance to a target comb shape $\tilde{A}_\mu^{\text{target}}$:

$$\mathcal{E}(\tilde{A}) = \sum_{\mu \neq 0} \left(|\tilde{A}_\mu| - |\tilde{A}_\mu^{\text{target}}| \right)^2 \quad (5)$$

This metric can be complemented to favour stable low-noise states, by adding the standard deviation of the mean comb power, estimated during the second half of the split-step evolution.

The raised-cosine comb spectrum shape is defined with the following expression:

$$\tilde{A}_\mu^{\text{target}} = \begin{cases} 1, & \frac{|\mu|}{\Delta} \leq (1 - \beta) \\ \cos^2 \left[\frac{\pi}{4\beta} \left(\frac{|\mu|}{\Delta} - (1 - \beta) \right) \right], & \left| \frac{|\mu|}{\Delta} - 1 \right| \leq \beta \\ 0, & \text{otherwise} \end{cases} \quad (6)$$

where Δ is the comb's 3-dB bandwidth and β is the roll-off factor, which controls the slope of the power decay in the outer lines of the comb.

Another metric can be used to ensure a minimum comb line power P_{min} over a given bandwidth Δ :

$$\mathcal{E}(\tilde{A}) = \sum_{\mu \in \Delta} \max \left(0, P_{\text{min}} - \frac{\hbar\omega_\mu D_1}{2\pi} |\tilde{A}_\mu|^2 \right) \quad (7)$$

In this way, comb lines exceeding the criterion are not penalized. A soft threshold function can also be used to force the power to be within a given range. The flat-top comb initial model follows the equation $A_\mu = A_0 / (1 + \mu/B)^8$, where B sets the bandwidth and A_0 the comb-line magnitude. A_0 was set to the maximum value authorizing convergence to a stable comb state.

In general, engineering the error function is a key aspect of inverse-design problems, and it requires careful consideration of the optimization goals, constraints and trade-offs. The two functions in equations (5) and (7) are two extreme cases when it comes to evaluating the comb's shape over a bandwidth of interest, as the former gives

equal weights to all comb lines, whereas the latter only accounts for the lines within a spectral region and disregards the lines outside. A more general approach is to introduce weight factors that reflect the importance of certain comb lines or regions of the spectrum. Alternatively, one could also use a weighting function that assigns higher importance to certain dynamics of the comb, to identify phenomena such as breathing.

Note that if the targeted problem is frequency-symmetric with respect to the pump, all odd dispersion coefficients can be set to zero and the optimization can be performed only on the even terms, reducing the number of variables while ensuring the symmetry of the solution.

At each iteration of the GA loop, a new population is created. First, the two best individuals from the last generation are carried over unchanged (elitism), which guarantees that the current optimum is preserved. Then, each new offspring is generated by selecting two (or more) parents at random, with a probability inversely proportional to their residual error, so that the fittest for the problem are selected more frequently (roulette wheel selection). The dispersion coefficients (genes) of the offspring are randomly selected from its parents (uniform crossover). The better the fitness of a parent, the more likely its genes will be selected. Finally, the offspring's genes are mutated by adding a random value drawn using a normal distribution with standard deviation σ . As the number of generation increases, σ is gradually decreased to favour the convergence of the algorithm.

Our genetic evolutionary algorithm was developed in MATLAB, without the use of existing optimization libraries. To speed up the steady-state intra-resonator field calculation, we implemented parallelization of the split-step Fourier-transform computations. This allowed us to substantially reduce the computation time, making the optimization process feasible within a few hours.

Mode-splitting calibration

The relation between the PhC amplitude, ρ_{PhC} , and mode splitting was calibrated experimentally on a series of single period PhCRs of identical base geometry (ring radius 109.5 μm , width 2 μm , height 570 nm), while the PhC amplitude ρ_{PhC} was swept. The results are shown in Extended Data Fig. 1. Note that the reported amplitude corresponds to the design value and not the measured geometry.

Although the relation is linear at small corrugation amplitudes, it reaches a maximum at ρ_{PhC} of ~ 200 nm for $\gamma/2\pi \sim 35$ GHz and the tuning direction reverses. We found that a near null splitting can be obtained for an ρ_{PhC} of ~ 420 nm, before γ increases again for larger amplitude values (Extended Data Fig. 1, inset). This counterintuitive bandgap closing was observed and explained by Gnan et al. in photonic wire Bragg gratings and is related to Brewster angle incidence⁴⁴ (it is also studied in ref. 22).

We did not observe any significant deviation from this calibration upon splitting multiple modes. Chirping the frequency components of the corrugation to reduce amplitude variations allows us to stay within the linear segment of this relationship and ensures a good replication of the splitting profile, as shown in Extended Data Fig. 2. Limiting the amplitude variations in the corrugation also avoids the need for high-aspect-ratio etching, which thus simplifies the nanofabrication of the PhCR.

Data availability

The data and code used to produce the figures of this manuscript are available on Zenodo at <https://doi.org/10.5281/zenodo.7998103>.

Code availability

The code for the genetic algorithm implementation used to perform the dispersion optimization is available at <https://github.com/ErwanLucas/inverseLLE>.

References

43. Hansson, T., Modotto, D. & Wabnitz, S. On the numerical simulation of Kerr frequency combs using coupled mode equations. *Opt. Commun.* **312**, 134–136 (2014).
44. Gnan, M. et al. Closure of the stop-band in photonic wire Bragg gratings. *Opt. Express* **17**, 8830–8842 (2009).

Acknowledgements

E.L. acknowledges support from the Swiss National Science Foundation (SNSF) under contract no. 191705. This research was funded by the DARPA PIPES programme under HRO011-19-2-0016 and the AFOSR FA9550-20-1-0004 project no. 19RT1019 and NIST.

Author contributions

E.L. implemented the optimization algorithm, performed the experiments and analysed the data. E.L. and S.-P.Y. contributed to the numerical simulations and resonators design. T.C.B. and D.R.C. fabricated the microresonators. E.L. wrote the manuscript, with input from all authors. S.B.P. supervised the project.

Competing interests

D.R.C. is a cofounder of Octave Photonics. The remaining authors declare no competing interests.

Additional information

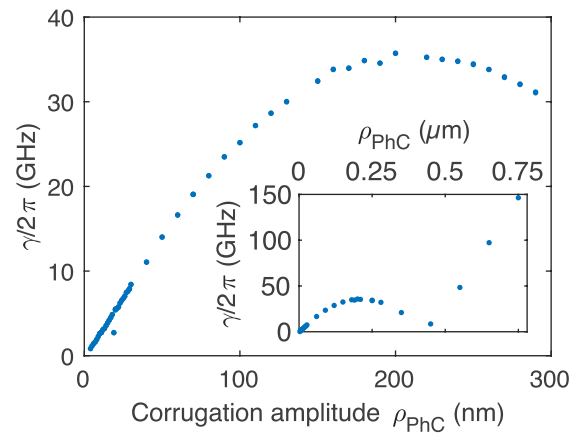
Extended data is available for this paper at <https://doi.org/10.1038/s41566-023-01252-7>.

Supplementary information The online version contains supplementary material available at <https://doi.org/10.1038/s41566-023-01252-7>.

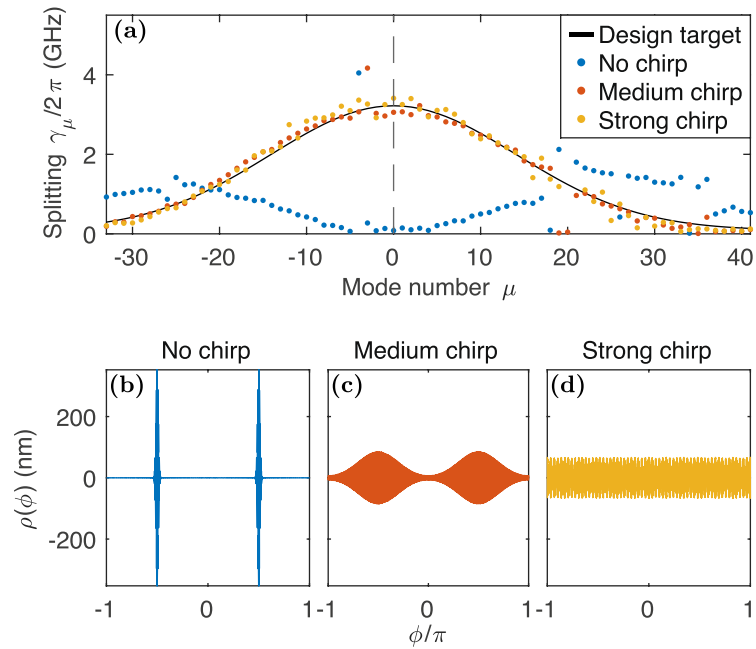
Correspondence and requests for materials should be addressed to Erwan Lucas or Scott B. Papp.

Peer review information *Nature Photonics* thanks Victor Torres-Company and the other, anonymous, reviewer(s) for their contribution to the peer review of this work.

Reprints and permissions information is available at www.nature.com/reprints.



Extended Data Fig. 1 | PhC and mode splitting calibration. Measured mode splitting of the target mode as a function of corrugation amplitude ρ_{PhC} (single frequency PhC), measured across 114 resonators. The inset shown an extended range of ρ_{PhC} .



Extended Data Fig. 2 | Effect of distributing the PhC pattern along the ring perimeter. (a) Measured mode splitting distribution with various amount of chirping applied to the corrugation pattern. The design target is the Gaussian

distribution shown in black. **(b-d)** Spatial profiles of the designed corrugations. **(a)** Without chirp, the splitting distribution is distorted and even inverted. The effect is avoided by chirping the pattern.